



Reactive Element Effect Applied by Alloying and SiHfBCN Coating on the Oxidation of Pure Chromium

Anke S. Ulrich¹ · Timo Kaiser¹ · Emanuel Ionescu² · Ralf Riedel² · Mathias C. Galetz¹

Received: 31 January 2019 / Revised: 10 July 2019 / Published online: 23 July 2019
© Springer Science+Business Media, LLC, part of Springer Nature 2019

Abstract

To reduce scale spallation, scale volatilization, and nitrogen embrittlement in Cr-based systems, reactive elements such as Y, Zr, Hf, La, and Ce were introduced as oxide dispersions into pure chromium. In addition, Hf coating systems were investigated. One was a Hf sputter layer with varying thickness, and the other one a Hf-containing precursor ceramic, i.e., SiHfBCN, which may be considered as suitable material for environmental barrier coating applications. Oxidation tests at 1050 °C in synthetic air for 50 h were carried out using thermogravimetric analysis. The samples were analyzed via X-ray diffraction, optical microscope, electron microprobe analysis, and scanning electron microscope. All reactive elements led to a decrease in total mass gain after oxidation compared to pure Cr, with Y and Zr showing the strongest effect. Improvements in oxide attachment, oxide growth rate, volatilization rate as well as nitridation resistance were observed. Concerning these experiments, Y showed the most promising results. Concerning Hf, coating systems, especially SiHfBCN, showed a higher effect on improving the oxidation resistance. The reason for this outcome might be that not only Hf is active in the precursor ceramic layer. A more complex oxide layer has formed, which consisted of not only Cr₂O₃ but also of Hf and Si oxides. This layer prevents the material from any nitridation under the selected oxidation conditions.

Keywords Chromium · Reactive element effect · Oxidation resistance · Impurity effect · Thermogravimetric analysis · Precursor ceramic SiHfBCN

This work was supported by the Deutsche Forschungsgemeinschaft (DFG) under Grant GA 1704/2.

✉ Anke S. Ulrich
ulrich@dechema.de

¹ DECHEMA-Forschungsinstitut, High Temperature Materials, Theodor-Heuss-Allee 25, 60486 Frankfurt am Main, Germany

² TU Darmstadt, Disperse Feststoffe, Otto-Berndt-Strasse 3, 64287 Darmstadt, Germany

Introduction

To improve turbine efficiencies by material developments, especially in aviation, two approaches are discussed in research and industry: reduction of weight either by using materials with higher specific strength compared to Ni-based superalloys, like TiAl alloys, or by using materials which offer higher melting points and therefore higher working temperatures. With regard to the latter, the most promising material group comprises refractory metals and refractory metal-based alloys. Among these, chromium and Cr-based alloys offer very interesting mechanical and physical properties, e.g., lower densities compared to those of Ni or Ni-based superalloys [1, 2], high thermal conductivity, and high oxidation resistance [3]. Another important point is availability, which is very high for chromium [4]. The main drawbacks preventing the use of Cr and its alloys in structural high-temperature applications so far are: (1) poor room temperature ductility, which is known to depend on the impurity content [5–8]; (2) embrittlement by nitrogen which enters the alloy during high-temperature oxidation ($T > 900\text{ }^{\circ}\text{C}$) [8–10]; (3) oxidation of pure Cr increases due to fast growing Cr_2O_3 scales, scale wrinkling and spallation at temperatures higher than $1000\text{ }^{\circ}\text{C}$ [11–13]. Concerning fundamental properties, the mismatch of thermal expansion coefficient (CTE) between pure Cr and Cr_2O_3 is higher ($2.6\text{--}2.5 \times 10^{-5} 1/^{\circ}\text{C}$ [2, 14]) compared to the mismatch in thermal expansion coefficient of Ni-based alloy and Al_2O_3 , which is around $5.1\text{--}6.6 \times 10^{-6} 1/^{\circ}\text{C}$ ($200\text{--}1000\text{ }^{\circ}\text{C}$) [15]. In addition, the Pilling–Bedworth ratio (PB ratio) of Cr_2O_3 formation on pure Cr is rather high for an oxide widely considered protective. Despite the inability to draw a simple correlation from both values to spallation resistance of the oxide, the occurrence of internal stresses in chromia is considered to be one of the biggest issues which might lead to increased spallation and cracking [16]. Reactive elements (REs) were repeatedly found to strongly suppress spallation from Al_2O_3 -forming alloys as well as from Cr_2O_3 -forming alloys. In addition, for the case of a balanced RE concentration there can be a significantly improved oxidation resistance of Al_2O_3 - and Cr_2O_3 -forming alloys, as already reported by Pfeil in the 1930s [17, 18]. Beside challenges in oxide scale formation, Cr also forms volatile species like CrO_3 which highly affect the oxidation kinetics at temperatures above $1000\text{ }^{\circ}\text{C}$ [12, 19, 20]. To the best of the authors knowledge, the effect of reactive elements on the volatilization of oxide scales has not yet been investigated.

The most prominent reactive elements which are known to have beneficial effects on the oxidation behavior of Cr_2O_3 and Al_2O_3 scales are yttrium, hafnium, cerium, zirconium, and lanthanum [21–24]. The reactive element effect (REE) was ascribed to four main points for chromium and Cr_2O_3 -forming alloys: (i) Enhancement of the selective oxidation by enhancing the diffusion of oxide-forming elements in the subsurface region most probably due to a decrease in oxide grain size; (ii) reduction of scale growth rate; (iii) change in scale growth mechanism from cation outward to oxygen inward transport; and (iv) improvement of scale adhesion [21–23, 25–27]. A change in chromia scale nucleation, grain size, and structure [28–30] might also lead to a change in scale morphology and

mechanical properties influencing the induced stresses in Cr_2O_3 during growth or thermal cycling. However, this effect is controversially discussed in literature [30–33].

Most experiments for investigating the REE were done on Al_2O_3 - or Cr_2O_3 -forming alloys while only little research was found on the investigation of the REE on pure Cr [29, 30]. To obtain the beneficial effects of reactive elements, the amount has to be kept very low in the range 0.01–0.5 wt.% [22]. Different ways of applying the REE on Cr and its alloys were reported, including: (i) addition of reactive element oxides as oxide dispersions (OD) [24, 26, 28, 34]; (ii) alloying with reactive elements [24]; (iii) ion implanting of RE into oxide scales [29, 35–37]; and (iv) surface coatings of reactive elements or their oxides [30, 38, 39]. OD are very interesting as they also influence the mechanical properties of the alloys [40] in contrast to surface layers. RE surface layers are introduced via different techniques: sol–gel deposition, sputtering, or chemical vapor deposition. The advantage of sputtering for RE oxide film production is the possibility to produce very thin but dense films on the substrate surface. Hussey and Graham [41] reported that a film thickness of only 4 nm is enough to provide the reactive element effect and that no further improvements in oxidation kinetics can be found for thicker sputtered films.

In this work, chromium was alloyed with small amounts of REs (Y, Hf, Ce, Zr, La) as oxide dispersions. This enabled a direct comparison of the different reactive element effects on pure chromium under the same oxidation conditions. Furthermore, two Hf-containing coatings were deposited on pure chromium to enable a comparison of different REE applications. The first one is a sputter coating, whereas the second system is amorphous polymer-derived SiHfBCN [42]. The latter was developed as a ceramic system that does not show any phase transition or decomposition up to 1400 °C and good oxidation resistance in the range of 1200–1400 °C [43]. Recently, the application of a polymer-derived coating consisting of Si–O–N on Mo–Si–B demonstrated an improvement of oxidation resistance at 800 °C and 1100 °C by forming an environmental barrier which additionally acts as oxygen trap [44]. Hence, it is expected that the SiHfBCN coating also improves the oxidation resistance of Cr. It is assumed to exhibit the properties not only of a silica former, but also of a reactive element supplier due to its Hf content, promoting stable, thermally grown oxide formation.

Experimental Procedures

For preparing the OD alloys, reactive elements were sputtered on 7-g chromium pieces (Cr > 99.95 wt.%, Plansee SE), which were subsequently melted by using electric arc melting. A RE concentration of 0.2 wt.% in each alloy was chosen based on the results of Pint [22]. Before sputtering, the Cr pieces were cleaned for 10 min in acetone using an ultrasonic bath and the size of the flat side, on which the RE were sputtered, was determined using optical microscopy and Imagic IMS analysis software. Reactive element sputter targets produced by Kurt J. Lesker Company (Y > 99.9%, Zr > 99.2%, Hf > 99.9% (ex Zr), La > 99.9%, Ce > 99.9%) were used. Previous to the experiments, a surface-dependent sputtering rate $S[\frac{\text{g}}{\text{cm}^2 \text{h}}]$ was deter-

mined (not shown here) following the dependence $S = \frac{\Delta m}{A \times t}$ in which Δm is the change in the samples' mass before and after sputtering, A the sputtered area, and t the sputtering time. With the help of the calculated sputtering rate, t was set according to the desired alloy composition ($t = \frac{m \times x}{A \times S}$, x is the weight fraction of the respect RE in the alloy, m the mass of the Cr sample).

For the sputtering process, the Cr pieces were additionally wrapped in Teflon foil so that only the measured side could be hit by the sputter particles. For deposition, radio frequency (RF) magnetron sputtering in a sputter coater (4-tec) was used, and the process was conducted in Ar (process gas flow 9 sccm Ar, 0.63 Pa for ignition). The applied power and the sputtering times were, respectively: Y: 0.21 kW, 59 min; Zr: 0.21 kW, 193 min; Hf: 0.22 kW, 79 min; La: 0.06 kW, 259 min; Ce: 0.11 kW, 173 min. Surface cleaning in an Ar-plasma was executed before the sputtering process (RF, 0.9 Pa, 30 W). After sputtering, the samples were alloyed by electric arc melting using the Compact Arc Melter MAM-1 by Edmund Bühler GmbH under an high-purity Ar atmosphere. In addition to the sputtered samples, a pure Cr sample was also fabricated by arc melting to obtain comparable impurity concentrations in all investigated samples. Prior to the sample melting, a zirconium sample was melted twice to getter oxygen from the melting chamber. To guarantee a homogeneous distribution of the RE in the alloy, the samples were remelted seven times. In addition to the previously mentioned sample, a pure Cr and a Cr–Y alloy were fabricated under the same conditions but using another Cr substrate with a higher purity (Cr > 99.995%). Such samples were prepared to identify the influence of RE on oxidation depending on different impurity levels in the substrate material.

Thermogravimetric analysis (TGA) was carried out to investigate the oxidation kinetics by measuring the change in mass gain over oxidation time. For the TGA experiments, small pieces of about $3 \times 8 \times 2$ mm were cut from the alloyed ingots via wire eroding, ground using SiC paper to a P500 surface finish, and cleaned in acetone for 10 min using an ultrasonic bath. The exact sample dimensions were measured via optical microscopy and Imagic IMS analysis software. The TGA setup consists of a Sartorius M25D-V precision balance, a programmable furnace (Carbolite CTE 15/75), and a cage made out of platinum wire covered with alumina tubes carrying the sample. The experiments were carried out at 1050 °C with a heating rate of $10 \frac{\text{K}}{\text{min}}$ and under a gas flux of $4 \frac{\text{l}}{\text{h}}$ in synthetic air, using Ar as protection gas for the balance. Prior to the experiments, the balance was stabilized for several hours in the gas flow to reach equilibrium. An oxidation time of 50 h at temperature was chosen because for pure chromium the first discontinuity in the mass gain characteristic can be found within this time [45]. Afterward, the furnace was let to freely cool down.

The sputter coatings were prepared on $9 \times 9 \times 13$ mm Cr samples. Hf was sputtered for 6 s, 12 s, and 18 s on each side to obtain different coating thicknesses which are in the range of 4 nm, 8 nm, and 12 nm (calculated values based on sputtering rate S). These thicknesses were chosen according to the findings of Hussey and Graham [41].

For deposition of the SiHfBCN coating, the spin coating process was chosen as it provides thin, dense, and homogenous layers on the surface of the substrate

and thus layer delamination can be avoided. The synthesis of the polymeric single-source precursor was performed in inert gas argon atmosphere. Thus, 10.8 ml of a commercially available polysilazane (HTT 1800, Merck KGaA) was dissolved in 20 ml anhydrous toluene. Subsequently, a solution of 4.8 ml of tetrakis(diethylamido)hafnium ($\text{Hf}(\text{N}(\text{Et})_2)_4$, Sigma-Aldrich) in 20 ml toluene was added dropwise at room temperature to the solution of HTT1800. The mixture was stirred for 2 h, cooled down to -50°C and then a solution of 2.4 ml of borane dimethyl sulfide complex ($\text{BH}_3 \cdot (\text{CH}_3)_2\text{S}$, Sigma-Aldrich) in 10 ml toluene was added dropwise to the cooled solution. After stirring for 2 h at -50°C , the solution was let to reach room temperature and stirred for 24 h. After the removal of the solvent in vacuum at $50\text{--}60^\circ\text{C}$, the preceramic polymer was obtained as a viscous liquid [46]. The obtained single-source precursor was dissolved in toluene (volume fraction 1:1.5) to get a solution with a viscosity suitable for the spin coating process and was applied onto chromium samples with the dimensions $9 \times 9 \times 2$ mm via spin coating (SPIN 150, SPS-Europe B.V.). The process took place under Ar atmosphere in a glove box. It was divided into three steps: (1) dispersion of the coating material all over the sample surface using a program of 10 s at 100 rpm with an acceleration of $500 \frac{\text{rpm}}{\text{s}}$; (2) actual coating step (30 s at 900 rpm with an acceleration of $500 \frac{\text{rpm}}{\text{s}}$); (3) removing the solvent from the coating for 30 s at 1000 rpm with an acceleration of $500 \frac{\text{rpm}}{\text{s}}$. After the spin coating process, a thermal treatment under argon atmosphere was done for cross-linking and pyrolysis. For cross-linking, the samples were heated from room temperature to 200°C for 3 h with a heating rate of $0.83 \frac{\text{K}}{\text{min}}$. Subsequently, the samples were heated to 1100°C for pyrolysis.

The sample coated with a Hf-based sputtered layer and the sample coated with amorphous SiHfBCN were isothermally oxidized in a tube furnace (Carbolite STF 14/450). The samples were put into Al_2O_3 crucibles and heated to 1050°C with a heating rate of $15 \frac{\text{K}}{\text{min}}$ in synthetic air with a gas flux of $4 \frac{1}{\text{h}}$ and a dwell time of 50 h with subsequent furnace cooling.

X-ray diffraction (XRD) analysis (Bruker D8 advance diffractometer, with Cu-K_α) is used for the identification of the coating compositions and of the oxides formed on the surface of the samples after oxidation. Bragg–Brentano geometry was used varying 2θ from 20° to 90° . For XRD pattern analysis, the PDF database was used.

Metallographic cross sections of samples in arc-melted condition, after spin coating, and after oxidation were prepared. A Ni coating was applied on the substrate surface using electroplating to protect the oxide scale. Subsequently, the samples were mounted in epoxy resin. The samples were ground with SiC paper and polished using diamond suspension up to a surface finish of $1 \mu\text{m}$ with a subsequent cleaning with acetone. The thickness of the oxide, nitride, and precursor ceramic layer was determined using optical microscopy. Thus, more than 20 measurements per sample were performed for at least three positions of the sample surface. The percentage of the areas which are directly in contact with the oxide were determined for selected samples using optical microscopy of the sample cross sections. At least three micrographs per sample were taken into account. Alloy composition and scale composition were investigated using electron probe microanalysis (EPMA, JEOL

JXA-8100) and secondary electron microscopy (SEM, Philips XL40 electron microscope) equipped with an energy-dispersive X-ray spectrometer (EDX).

Results

Arc-melted Microstructure

As an example of the microstructure after arc melting, a BSE image and corresponding element maps for the Cr–0.2 Hf [wt.%] sample are shown in Fig. 1. All samples consist of a Cr matrix with homogeneously distributed reactive element-containing precipitates. EPMA point measurements (not shown here) indicated that these precipitates are fully oxidized and therefore are inferred to be Y_2O_3 , ZrO_2 , HfO_2 , La_2O_3 , or CeO_2 . As reactive elements have a very high affinity to oxygen, the oxidation occurred during the sputtering process and arc-melting.

Effect of Different Cr-based Material Purities on Oxidation Behavior

To investigate the influence of impurities in the base material, pure Cr and Cr–Y alloys made of two different commercially available Cr materials, but produced under the same conditions, were oxidized using the TGA setup. For the pure material, no significant influence of the material purity was found on the total mass gain (see Fig. 2). Both showed a nearly identical mass gain after 50 h at 1050°C in synthetic air which is $8.01 \frac{mg}{cm^2}$ for 99.95 wt.% Cr and $8.34 \frac{mg}{cm^2}$ for 99.995 wt.% pure Cr. However, the slope of each plot and therefore their oxidation characteristics differ to some extent. Looking at the cross sections of the samples after oxidation (Fig. 3) Cr_2N layers with characteristic Cr stripes [45] are found at the surface. The Cr_2N was also confirmed by XRD (not shown here). The average nitridation depth is $65 \pm 6 \mu m$ and $88 \pm 14 \mu m$ for the 99.95 wt.% Cr and the 99.995 wt.% Cr,

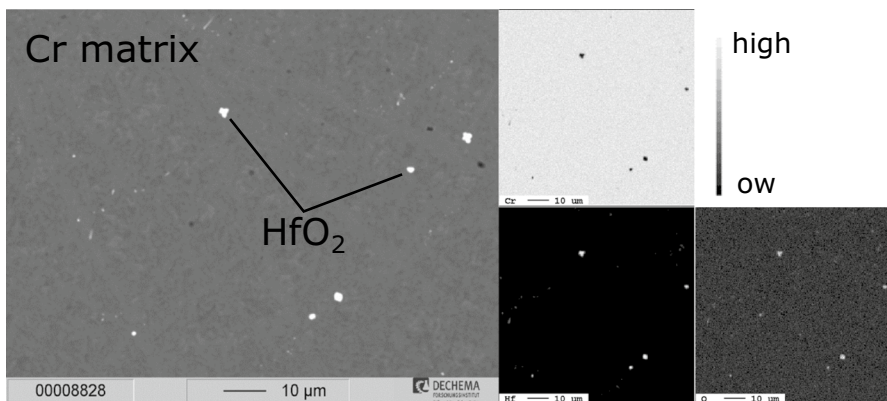


Fig. 1 BSE image (left) and corresponding EPMA element maps of Cr, Hf, and O of the Cr–0.2 Hf alloy [wt.%]

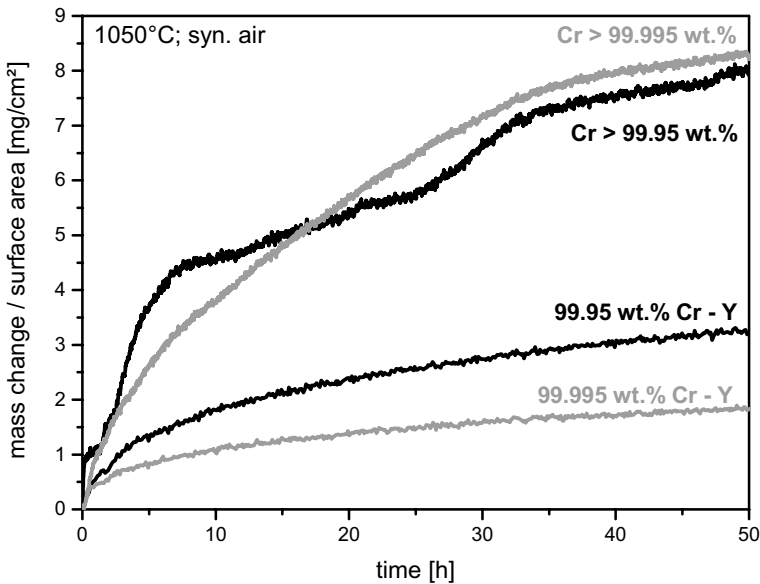


Fig. 2 Thermogravimetric measurements showing the mass change per surface area for pure Cr and Cr-0.2 Y samples with different purities. Oxidation is carried out for 50 h at 1050 °C

respectively. Concerning the oxide layer which usually forms on Cr and its alloys, both pure samples showed complete oxide scale spallation after cooling and sample preparation (Fig. 3).

For both Cr types, the addition of 0.2 wt.% Y led to lower mass gains per surface area, a remaining Cr_2O_3 oxide scale (also proven by XRD which is not shown here) after the TGA measurement, and a thinner layer of Cr_2N below the oxide scale (both also shown in Figs. 2, 3). For the higher-purity sample, the effect is more pronounced compared to the lower-purity sample. The tendency for gap formation between metal and oxide scale was investigated by determining the percentage of the areas which are directly in contact with the oxide. For the 99.95 wt% Cr alloy, it is $22 \pm 12\%$; for the 99.995 wt% Cr alloy, it is $96 \pm 1\%$.

Considering the TGA measurements, both alloys containing Y do not show any rapid mass changes (perturbations). Another difference between the two Cr–Y samples is that the oxide scale of the lower-purity alloy (Cr 99.95 wt%–Y) is partly detached from the surface, while the oxide scale found on the high-purity sample remains attached to the sample over the whole surface. In addition and noteworthy, the 99.995 wt.% Cr–Y sample showed no Cr_2N formation below the oxide scale after an oxidation of 50 h at 1050 °C in synthetic air.

Oxidation Kinetics of OD Cr Alloys Containing 0.2 wt.% RE

The resulting TGA curves measured at 1050 °C in synthetic air are shown for the RE-doped samples and the pure chromium sample (99.95 wt.% Cr) in Fig. 4. All

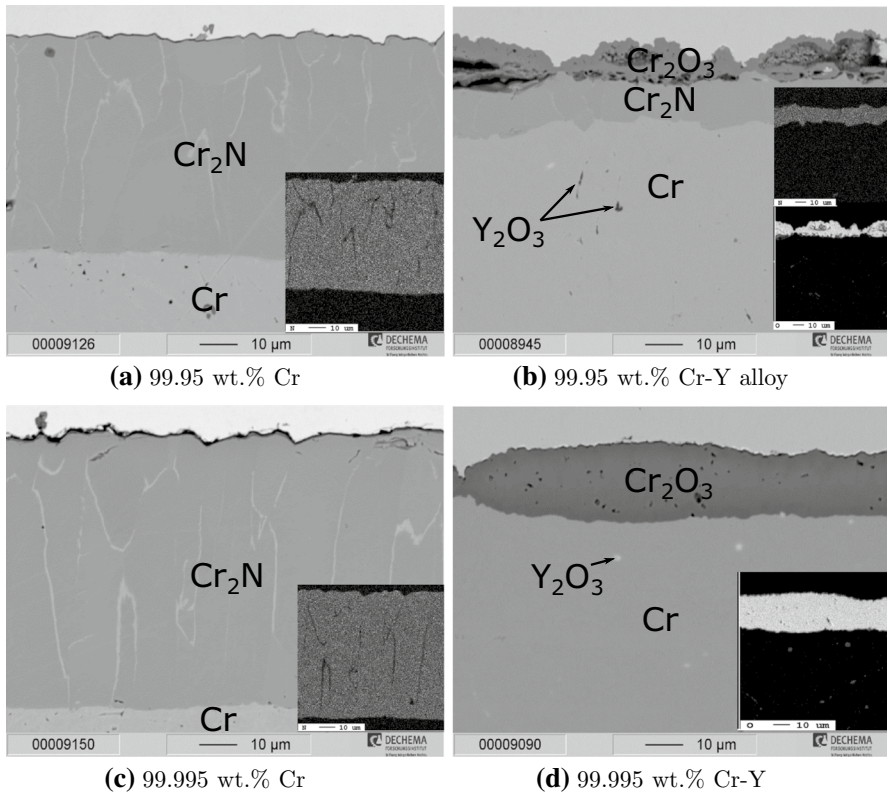


Fig. 3 Cross section of pure Cr samples and Cr–0.2 Y samples with different purities after oxidation for 50 h at 1050 °C in synthetic air

tested reactive element additions led to a lower mass change per surface area after 50 h of oxidation compared to the pure chromium sample. Y and Zr showed the highest impact on the mass change. Alloying with Y suppressed rapid mass gain and discontinuities in the mass gain characteristics, while the addition of Zr led to an even lower mass gain in the beginning of the oxidation experiment. However, after around 36 h and 40 h, Cr–0.2 Zr showed rapid mass gains and the mass gain rate accelerates.

In Fig. 5, the cross sections of the samples after oxidation are shown except for the Cr–0.2 Y alloy, which was already shown in Fig. 3 together with the pure 99.95 wt.% Cr.

In contrast to pure Cr, the oxide layer of the Y-alloyed sample remained attached to the substrate even though both samples experienced the same cooling rates. On Cr–0.2 Zr and Cr–0.2 Hf, only parts of the scale were attached to the substrate, while the oxide scales formed on Cr–0.2 La and Cr–0.2 Ce spalled completely after oxidation. This spallation happened during cooling as no indication for spallation (perturbation) was observed in the TGA plots.

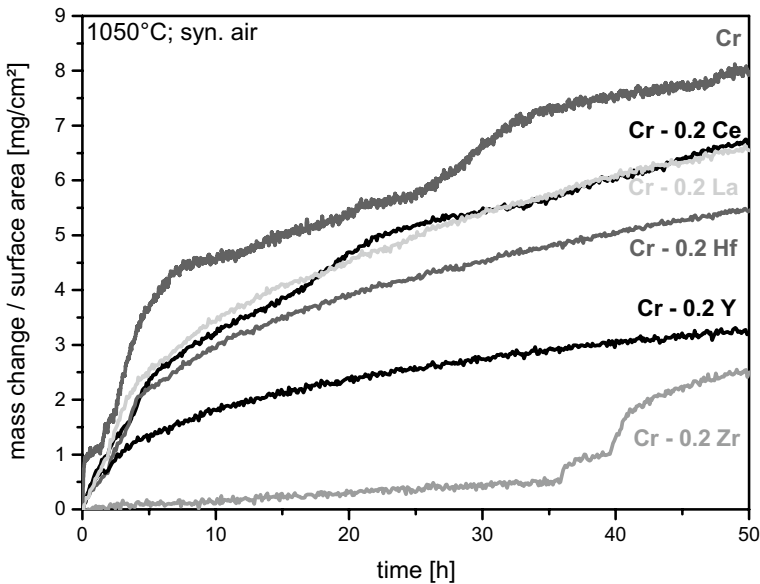


Fig. 4 Mass change per surface area over time of the different Cr–RE alloys compared to the pure Cr sample (purity 99.95 wt.%). The addition of all reactive elements leads to decrease in mass gain during oxidation and therefore to an improvement of oxidation resistance

For a more detailed investigation of the effect of Zr at shorter oxidation times, cross sections of Cr–0.2 Zr alloy after 20 h oxidation (same conditions) are shown in Fig. 6. Figure 6a shows the typical appearance of the surface area. No Cr_2N has formed below the oxide scale. However, locally in the presence of cracks in the oxide scale a thin nitride layer has formed (compare Fig. 6b). As no rapid mass gain occurred during the 20-h exposure (TGA plot not shown here), during the cooling, the formation of Cr_2N is assumed to take place during the cooling process after exposure. The percentage of the substrate surface which is directly in contact with the oxide was determined for both Cr–0.2 Zr samples and is $10 \pm 8\%$ for the sample oxidized for 20 h and $19 \pm 2\%$ for the sample oxidized for 50 h.

Thickness measurements of the Cr_2N layer and the attached oxide scales are displayed in Fig. 7. The oxide layer shows oxide thicknesses in the range of around 7–12 μm . The thickness of the nitride layer decreases with RE addition except in the case of Ce alloying. Both scale thicknesses follow the trend of the mass gain values of the TGA measurements. The results show that an attached oxide scale leads to a thinner Cr_2N layer, and a thinner Cr_2O_3 scale corresponds to a thinner nitride layer.

To rank the oxidation resistance of the alloys and to analyze the oxidation kinetics, the TGA characteristics are fitted using Eq. 1 [20]:

$$\frac{\Delta m}{A} = (k_p \times t)^{0.5} - k_v \times t \quad (1)$$

where k_p is the parabolic rate constant and k_v is the volatilization rate constant. k_p includes all mass gains due to Cr_2O_3 formation as well as due to Cr_2N formation as

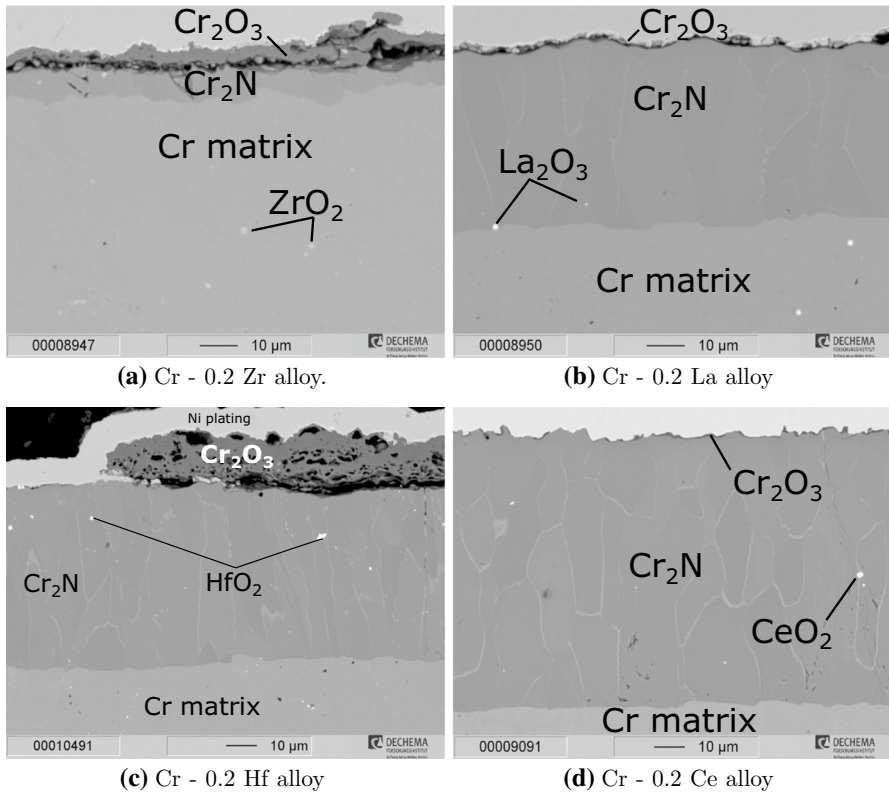


Fig. 5 BSE images of the surface area of the alloyed samples after oxidation for 50 h at 1050 °C in synthetic air using TGA

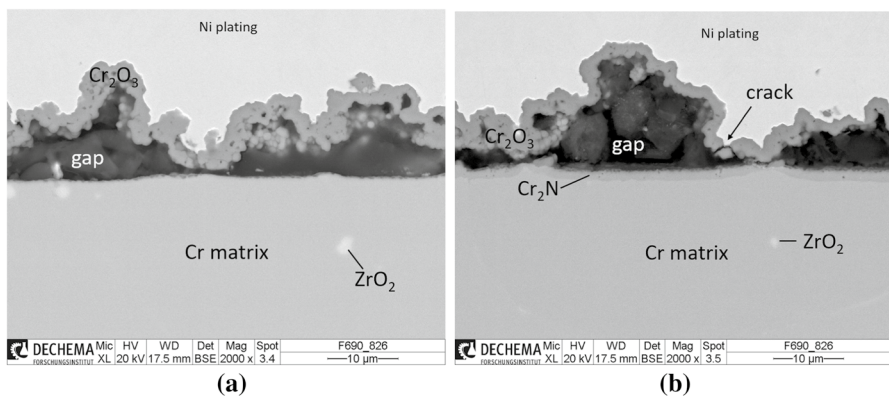


Fig. 6 BSE images with higher magnification of the surface area of the Cr–0.2 Zr alloy after oxidation for 20 h at 1050 °C in synthetic air. **a** is an example for the majority appearance of the surface area while in **b** a certain spot is shown where Cr₂N has already formed. Its formation is assumed to happen during the cooling of the sample

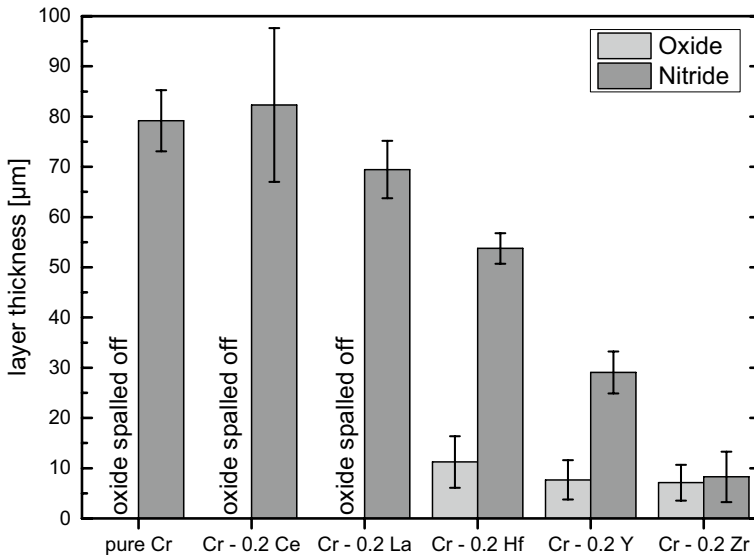


Fig. 7 Illustration of the average oxide and nitride layer thickness and the corresponding standard deviation. The alloys are sorted according to decreasing mass gain per surface area during TGA experiments

both itself are parabolic [47, 48] as well as the oxidation of Cr_2N resulting in Cr_2O_3 formation [10]. k_v covers all effects of formed volatile species such as Cr and CrO_3 which cause a linear mass loss over time [3, 49]. This formula differs from the commonly known parabolic oxide growth because for chromium the parabolic rate law can only be applied for temperatures up to the range of 800–900 °C in dry air [11, 50]. For fitting the Cr–0.2 Zr kinetics, only the time up to the first discontinuity (around 36 h) is taken into account. The reason for such discontinuities are local scale failures [45, 51], which cannot be taken into account using this fit.

The calculated fit values and the corresponding R^2 values are listed in Table 1.

Table 1 Analysis of the growth kinetic of the different RE-alloyed samples with respect to Eq. 1

Sample	$k_p/10^{-10}\text{g}^2\text{cm}^{-4}\text{s}^{-1}$	$k_v/10^{-8}\text{gcm}^{-2}\text{s}^{-1}$	R^2 -value
Cr	6.50 ± 0.03	1.58 ± 0.02	0.97
Cr–0.2 Ce	3.30 ± 0.04	0.54 ± 0.03	0.99
Cr–0.2 La	3.74 ± 0.04	0.88 ± 0.03	0.99
Cr–0.2 Hf	2.91 ± 0.04	0.98 ± 0.03	0.99
Cr–0.2 Y	1.18 ± 0.01	0.75 ± 0.01	1
Cr–0.2 Zr	$0.28 \text{ E-}3 \pm 0.13 \text{ E-}3$	-0.36 ± 0.01	0.94

The purity of the used Cr is > 99.95 wt.% in all cases

Oxidation Resistance of the Hf-Based Sputtered Coating

Due to the small thickness of the sputtered layer, it could not be investigated in detail (layer thickness, morphology) by the used analyzing techniques. However, XRD measurements done on a sample with a thicker Hf sputter coating (sputtered for 30 min, not shown here) demonstrated the deposition of Hf. A thin Hf layer in the dimensions of nm is expected to be oxidized as soon as it is exposed to air due to the high HfO_2 stability. As no coating thickness could be determined, the sputter time is given instead of an actual layer thickness. However, the effect of the sputter layer deposition is obvious by looking at the sample surfaces after oxidation for 50 h at 1050°C in synthetic air (see Fig. 8). Increasing the Hf sputter time and thereby increasing the sputter layer thickness improves the attachment of the oxide scale after oxidation. The different sides are named as following: S1 indicates the shortest sputter time and therefore the thinnest Hf sputter layer, S2, is the medium, and on S3 Hf was sputtered longest.

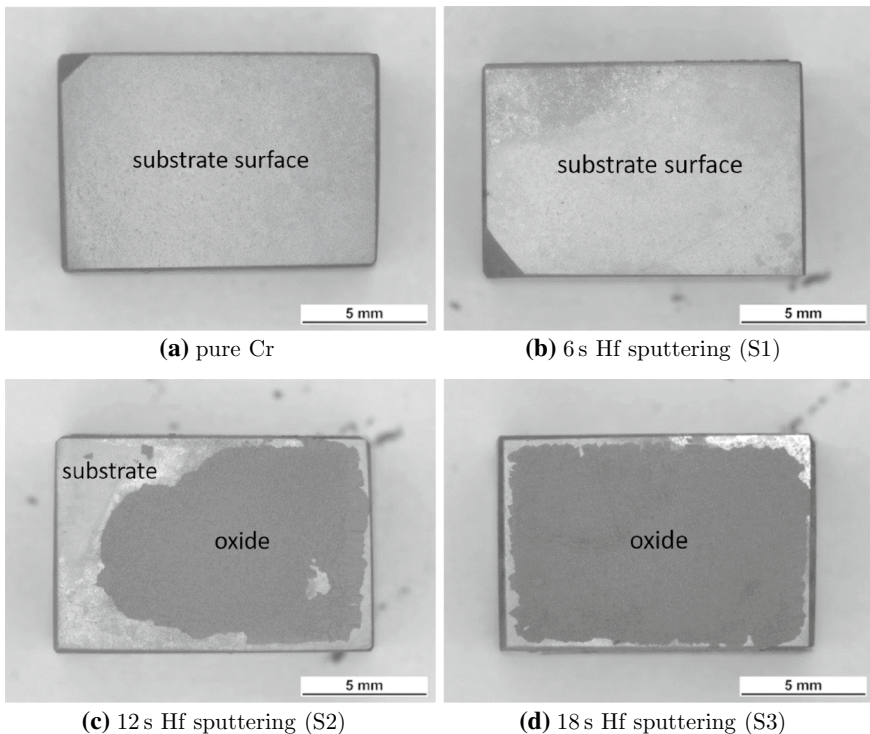


Fig. 8 Optical micrographs of pure chromium (a) and chromium coated with Hf sputter layers (b–d) after oxidation at 1050°C for 50 h in synthetic air. The different sputter layer thicknesses are indicated by the respective sputter times of Hf

The effect of the Hf coating on the Cr_2N and Cr_2O_3 layer thicknesses is shown in Fig. 9, together with a BSE cross section of the longest sputtered side S3, indicating the formation of both layers.

Precursor Ceramic Layer and Oxidation Performance

The Cr sample coated with amorphous precursor-derived SiHfBCN coating is shown in Fig. 10a. The ceramic coating has the chemical composition $\text{SiHf}_{0.1}\text{B}_{0.18}\text{C}_{0.72}\text{N}_{0.89}\text{O}_{0.1}$ and a thickness of ca. 1.3 μm . No Cr is found in the area of coating layer with respect to EPMA point measurements (not shown here) and the EPMA Cr element map in Fig. 10a. This indicates that there is no extensive interdiffusion between the Cr substrate and the SiHfBCNO layer during the ceramization of the preceramic polymer. Using the described process parameters, a homogeneous, attached, and dense coating is formed on Cr substrate except for the sample edges due to the process setup. However, these edges are not taken into account in the following.

After the oxidation of the SiHfBCN-coated sample at 1050 °C for 50 h, still an adherent scale exists on the substrate. The EPMA results indicate that the precursor-derived ceramic layer is sandwiched by two layers which seem to consist mainly of chromia. According to the XRD pattern of the oxidized sample (Fig. 10c), the coating consists of monoclinic hafnia and small amounts of SiO_2 cristobalite as crystalline phases together with Cr_2O_3 eskolaite. With respect to former studies on monolithic SiHfBCN, the scale formed after oxidation can be described as consisting of hafnia nanoparticles dispersed in a glassy borosilicate matrix [52]. Interestingly, N can only be detected locally in the sample subsurface demonstrating a high resistance of the coated sample to Cr_2N formation. This can be correlated to a very low diffusivity of species through the precursor-derived ceramic coating. Recently, it was shown that the diffusivity values of Si, Hf, and C in Si(Hf)OC are around $10^{-21} \frac{\text{m}^2}{\text{s}}$, $10^{-21} \frac{\text{m}^2}{\text{s}}$, and $10^{-18} \frac{\text{m}^2}{\text{s}}$, respectively [53–55] at 1300 °C indicating that this

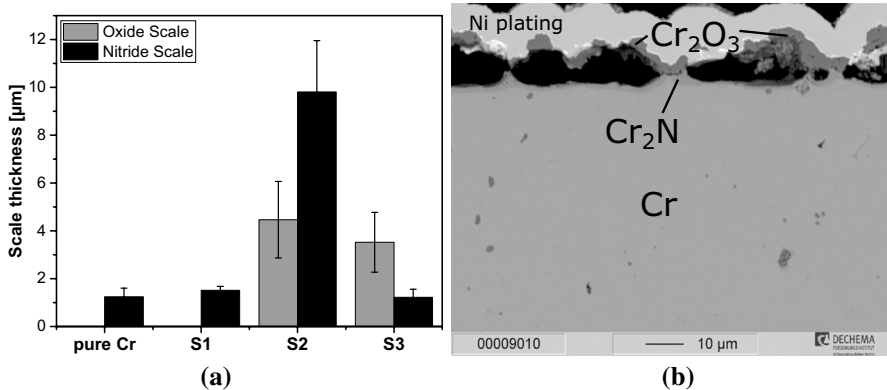
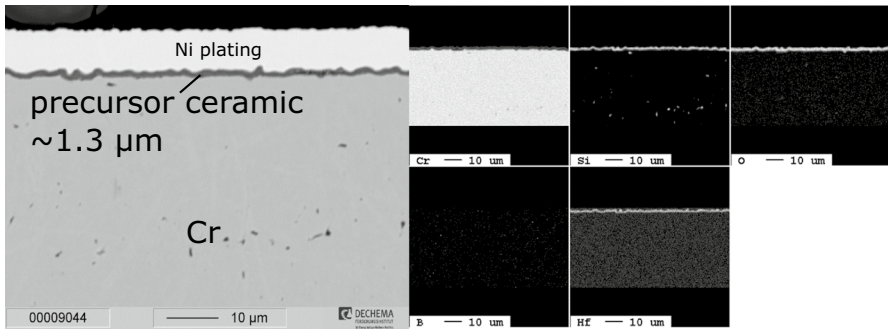
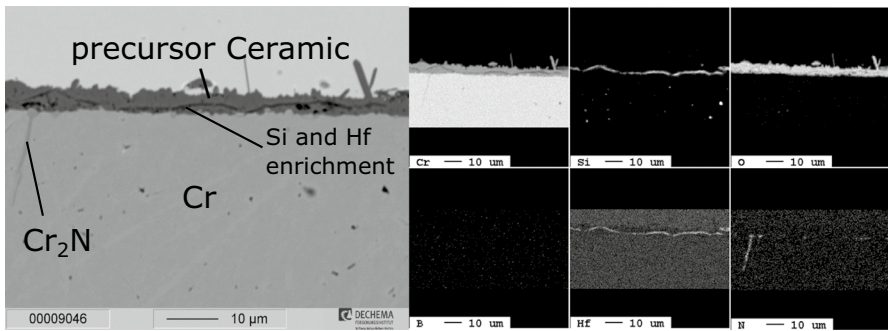


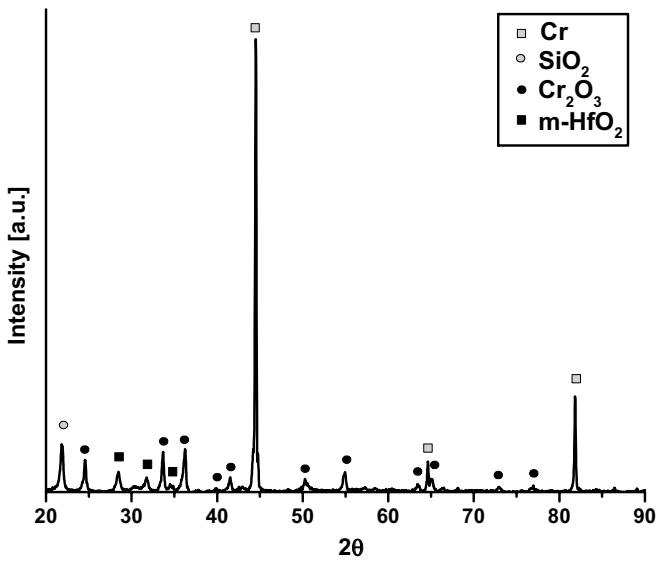
Fig. 9 Investigations on the Hf-sputtered samples. In **a**, the layer thicknesses of Cr_2O_3 and Cr_2N over increasing Hf sputter layer thickness is shown. A corresponding BSE image of the cross section of the S3 side is found in **b**



(a)



(b)



(c)

Fig. 10 BSE image and corresponding element maps of a cross section of the precursor coated sample after coating deposition (a) and after oxidation for 50 h at 1050 °C in synthetic air (b). In addition a XRD pattern of the oxidized sample's surface is shown in (c) indicating the formation of mainly three different oxides

type of material may be suitable as barrier coating against oxidation at high temperatures [52, 56, 57].

Discussion

Effect of Base Material Purity on Oxidation Performance

In the literature, it is found that impurities play a major role in Cr-based alloys, affecting the mechanical properties as well as oxidation behavior [5, 58, 59]. This is the reason for the comparison of two different chromium materials, pure and alloyed with 0.2 wt.% Y, with different purities. As it is assumed that the concentration of impurities such as N, O, C, and probably H is increased during arc melting, also the pure Cr alloys were fabricated using arc melting.

The results show no significant influence of the materials purity on the TGA curve without a RE addition. The average nitridation depth in both cases is higher than 60 μm and the oxide scale spalled off after oxidation for both chromium samples. This is different for the Y-alloyed samples. The alloys containing 0.2 wt.% Y indeed showed a drastic decrease in mass gain per surface area. However, the influence of RE is much higher for the Cr sample compared to the lower-purity alloy. The oxide scale of 99.995 wt.% Cr–Y is completely adherent to the sample, while the oxide scale of the 99.95 wt.% Cr–Y sample shows wrinkling and gap formation between sample surface and oxide scale. As described by Whittle and Stringer [26], the bonding between metal and oxide scale can be weakened due to the influence of impurities that segregate at the metal/oxide interface and promote void formation or decrease the chemical bonding. The reactive elements prevent the impurities from segregating to the interface by interacting with them and forming stable compounds so that void formation is inhibited and the interface stays strong. The only difference between both alloys is the different concentration of impurities. O, N, Na, C, and especially S are generally considered as elements influencing scale adhesion performance of Al_2O_3 scales in particular [22, 23]; however, little knowledge about the effect on Cr_2O_3 is available. The most popular mechanism is the “sulfur effect” [26]. The hypothesis to start from is that the metal/scale interface is intrinsically strong. Indigenous sulfur and other impurities present in metals and alloys can segregate to the metal/scale interface during oxidation. This segregation seems to promote interfacial void formation but can also weaken the chemical bonding between oxide and scale [22]. This segregation is inhibited by RE additions [21] leading to a stronger scale/substrate adhesion; however, these effects seem to be less important for Cr_2O_3 scales [60]. Both Cr-based materials were highly different in their C, N, S, and O contents which means that the concentrations of C, S, and O are much higher in the Cr 99.95 wt.% material compared to the Cr 99.995 wt.% material (the amount of S in Cr 99.95 wt.% is at least three times, O and C at least twice).

As 99.995 wt.% Cr has a lower concentration of impurities, less Y might be necessary to getter the impurities and avoid interface segregation. In other words, the fraction of impurities gettered by Y might be higher for the high-purity alloy than for the lower-purity alloy [22]. This leads to an adherent oxide scale which

is not negatively influenced by void or gap formation, while for the lower purity Cr–0.2 wt.% alloy, the amount of Y is not sufficient to completely avoid segregation of impurities to the interface and void formation so that the oxide scale loses contact to the metal surface at some points. To verify, alloys fabricated with varying Y concentration to impurity ratio would be interesting to investigate in future.

Investigation of Oxidation Kinetics

As seen in Table 1, mass gain as well as mass loss during oxidation experiment are decreased by alloying Cr with reactive elements. Y and Zr seem to act superior; however, Ce which was expected to highly improve the oxidation resistance [41] shows less promising results. The reason might be the different application of RE in [41], as Cr was coated with several RE oxides. Interestingly, Y seems to be not affected by this difference. As summarized in several reviews, the decrease in the parabolic oxidation rate by RE addition has often been reported for Cr₂O₃ formers [22, 23, 26]. With respect to pure Cr, the simultaneous decrease in evaporation rate of volatile species formed during oxidation is very interesting. The change in oxide growth mechanism from cation outward diffusion dominated scale growth to oxygen inward dominated scale growth by RE addition is one of the most common postulations [23]. Thereby the oxide morphology is also changed [61] which could have an effect on the formation of volatile species resulting in a decreased k_v . The reason is mostly assumed to be RE segregation at Cr₂O₃ oxide grain boundaries [29, 35, 62, 63]. However, to detect the RE at their low amounts requires advanced imaging techniques.

Investigating all alloyed samples, all except Cr–0.2 wt.% Zr showed parabolic mass gain characteristics and k_p , as well as k_v , are decreased by RE addition. Cr–0.2 wt.% Zr seems to have other oxidation kinetics compared to the other reactive element alloys at least before the first rapid mass change at around 36 h. Instead of a linear mass loss, linear mass gain is found in addition to parabolic mass gain. It has to be mentioned that this type of fitting is only a technical fitting and k_p and k_v cannot directly be compared to the physical meaning of these constants as in Cr and Cr-based alloys several species are formed leading to mass gain as well as mass loss. However, the values give a trend showing that the mass gain characteristic changes for Cr–0.2 Zr alloy to linear. In Fig. 6, additional cross sections of an oxidized Cr–0.2 Zr alloy after 20 h are shown. It is found that nearly no Cr₂N has formed below a close, highly wrinkled, and detached Cr₂O₃ scale which indicates that the measured mass gain is only related to Cr₂O₃ formation. As the scale has wrinkled and detached, the surface area has highly increased during oxidation resulting in a linear mass gain term. Volatile species most probably form, but their effect on the mass gain characteristic seems to be much lower compared to the linear high increase.

All reactive elements except Zr prevent rapid mass change discontinuities at least for 50 h at 1050 °C. These perturbations are well known from Cr₂O₃ formed on pure

Cr. They are mainly attributed to Cr_2N formation due to local oxide scale failure [68].

For pure Cr, an atomic size effect could not be seen in this study. Even though a close atomic percentage of alloying elements is added to Cr–0.2 Hf, Cr–0.2 Ce, and Cr–0.2 La as well as for Cr–0.2 Y and Cr–0.2 Zr no comparable correlation as shown by Pint [22] was found. This might be attributed to the fact that the investigated alloy Ni-25 wt.% Cr solely forms an oxide scale while on Cr–0.2 wt.% RE alloys the weight gain during oxidation is caused by Cr_2O_3 and Cr_2N formation.

Influence of Reactive Element Addition on the $\text{Cr}_2\text{O}_3/\text{Cr}$ Interface

A very important factor to mention is that the change in oxide scale growth behavior and especially oxidation rate also influences the attachment of the oxide scale. It is well known that the oxide thickness plays a major role as thicker oxide scales tend to spallation. Hence, a decrease in growth rate by for example the hindrance of Cr cation and O anion grain boundary diffusion upon RE segregation to the grain boundaries in the scale [22, 29, 36, 65–67] highly reduces the probability of oxide spallation or detachment. This is also demonstrated in this study, since a decrease in oxide scale thickness of Hf-sputtered samples (see Fig. 9a) leads to a decrease in oxide scale spallation (Fig. 8).

Comparing both Cr–Y alloys with different Cr purities, the oxide scales highly differ (see Fig. 3). Linking oxide scale appearance and kinetic investigations, it is found that a lower overall mass gain after exposure, which means an improved oxidation and especially nitridation resistance, goes along with a continuous connection between substrate and scale. This in turn highly depends on the purity of the material. However, for the Cr–0.2% Zr alloy it is the other way round: After 20 h of oxidation, the oxide scale is only loosely bound to the substrate (surface area of a direct Cr/ Cr_2O_3 contact is $10 \pm 8\%$) but no nitridation occurred. As wrinkling and detachment are signs for high induced stresses in the oxide scale during growth, the scale seems to have a high level of internal stress. After 50 h, an increased scale attachment is found but also increased nitridation of the substrate. The increase in surface attachment seems to contradict findings of Li and Hou [61] who claimed that the size of voids which form at the $\text{Cr}_2\text{O}_3/\text{Cr}$ interface and thereby the detachment of the scale increases with increasing oxidation time. Considering the perturbations in the TGA plots, heavy scale spallation occurred between 20 and 50 h leading to regrowth of the oxide scale. This in turn is the reason for the increase in connections between oxide scale and substrate with longer oxidation times. Therefore, the results do not exclude the growing of interfacial voids as in this case only an intact oxide scale has to be considered. The large mass gain discontinuities observed using TGA are abrupt and refer to a high substrate surface area which is spontaneously exposed to air. This is only possible if the scale was already detached or only loosely and locally attached to the substrate surface before local destruction or spallation. Thereby, air can access the gap between substrate surface and oxide scale. Cr_2O_3 and Cr_2N are formed simultaneously on a rather large area leading to a high spontaneous mass gain. To investigate the reason for the difference in oxidation and spallation

behavior of Cr–0.2 Zr and the other RE-alloyed samples, diffusion experiments are suggested as starting point. Thereby it can be investigated if the oxide growth kinetics are changed by RE doping and if this results in a change in gap formation between Cr_2O_3 and the substrate.

The Role of Nitridation

Figure 6 shows that Cr_2N formation is related to the appearance of the Cr_2O_3 scale. In the case of cracks, nitrogen can penetrate the oxide scale and form nitrides. Based on these results and the molecular nitrogen transport model [68], it is assumed that an intact oxide scale is able to prevent the substrate from nitridation. This is in accordance with recent studies by Dorcheh et al. [48] who claimed that a close and adherent oxide scale is a barrier for nitridation. The formation of cracks in turn is affected by stresses in the oxide scale. Increased stresses occur for example during cooling but are also related to the oxide scale morphology and growth direction.

Additionally, nitridation also depends on the scale/metal interface appearance. An intact $\text{Cr}_2\text{O}_3/\text{Cr}$ interface precludes nitridation which is shown by the oxidation of 99.995 wt.% Cr–0.2 Y (compare Fig. 3d) and of the precursor coated and oxidized sample (see Fig. 10b). Another evidence for the interaction of oxide scale and nitridation is found with regard to the Hf-sputtered samples. The Cr samples sputtered with Hf S1 and S3 both show thinner nitride layers in comparison with S2. In comparison with S1, the reason is that no attached oxide scale was found on the substrate after oxidation. This oxide scale spalled off either during oxidation or during cooling or both in combination. Anyway, a weak $\text{Cr}_2\text{O}_3/\text{Cr}$ bonding is assumed leading to nitridation of the base metal. It is important to note that Cr_2N is not stable in air [48] and its oxidation rate was found to be comparable to that of pure chromium at 1000 °C [10]. Hence, the Cr_2N thickness decreased due to oxide formation which spalled off again. By increasing the Hf concentration at the substrate surface, the oxide becomes more protective which is also demonstrated by the remaining oxide scale after the exposure. Less Cr_2N is oxidized and a thick nitride layer is observed for S2. A thicker Hf sputter layer further decreases the permeability of the oxide scale for N in air resulting in a thinner nitride scale below an adherent oxide scale. A thinner Cr_2N scale thickness and therefore lower nitrogen uptake goes along with a decrease in oxide thickness which is also found for the alloyed systems (compare Fig. 7). Thickening the Hf sputter layer seems to improve the oxidation resistance; however, it is well known that adding RE over a critical content results again in a decrease of oxidation resistance [22, 69]. Further investigations should deal with the threshold for RE overdoping in the Cr-based system.

All Cr–RE alloys showed nitride formation but only alloying with Zr led to rapid mass changes indicating nitridation. The mechanism is assumed to be the following: As the partial pressure of Cr at 1050 °C is already high, gaseous Cr is believed to be present below the scale [64]. In the case of scale failure, its oxidation can close the scale again; however, the remaining nitrogen below the scale forms Cr_2N which is stable at a low oxygen partial pressure [3]. As synthetic air consists of around 80% N_2 and only 20% O_2 the huge mass gain caused by local scale failure and visible

as discontinuities in the TGA curves is assigned to Cr_2N formation. The mass gain in turn is proportional to the volume of synthetic air below the oxide scale; hence, it also depends on gap formation. However, in the case of continuous mass gain during TGA accompanied by nitride formation as it is observed for OD alloys except Zr, a constant supply of N to the Cr metal has to be present. This is most probable due to numerous and continuously distributed oxide scale failures (compare Fig. 5), but also other mechanisms such as N diffusion via oxide grain boundaries in the way it is proposed for C penetration through oxide scales [70] cannot be ruled out.

Comparison of Alloying and Coating of Reactive Elements or SiHfBCN

The precursor ceramic samples represent a special case regarding the reactive element effect. Hf is present in the precursor layer in a quite high concentration of around 2.5 at% Hf. After SiHfBCN deposition process, the sample shows no interaction with the coating; however, after oxidation the formed scale differs from the scale formed on the precursor ceramic itself at 1200–1400 °C [43]. The main difference is the formation of Cr_2O_3 in this study. Hence, a reaction of the coating with the underlying material occurs during oxidation but not during coating deposition; however, the exact mechanism is not known yet. Comparable to [43] SiO_2 (cristobalite) and monoclinic HfO_2 also formed indicating an oxidation of the precursor layer. The formed scale shows good attachment to the substrate which in turn shows highly decreased nitridation attack. The reasons for this could be related to the reactive element effect of Hf but also to the development of a duplex oxide scale (Cr_2O_3 and oxidized precursor) which seems to be a promising approach for improvement of oxidation resistance of Cr-based alloys [71]. In addition, Hou and Stringer stated that the most effective RE coatings are those which are the densest and most continuous [72]. The SiHfBCN itself is continuous and dense after deposition, which is considered to have a positive effect on the oxidation resistance of the coated sample. As the elements B, C, and N have low concentrations and cannot be detected in the ceramic layer using EPMA; their influence on the adhesion of the scale cannot be determined. For the investigation of the precursor ceramic development during oxidation and its lifetime, further oxidation experiments with longer oxidation times and cyclic temperature changes should be conducted in future.

By comparing Cr–0.2 wt.% Hf (see Fig. 5c), the Hf-sputtered sample (see Fig. 9b) with the SiHfBCN-coated Cr sample (see Fig. 10b), it is found that on the alloyed sample both thickest oxide as well as nitride layer have formed after oxidation. Both coating systems differ in the amount of Hf, with the sputtered Hf sputter coating having an overall lower concentration compared to the SiHfBCN coating. On the precursor ceramic-coated sample, a thicker oxide scale has formed compared to the Hf-sputtered sample; however, no nitride formed below. This can be attributed to the barrier effect of the coating and increase in REE due to a higher Hf concentration at the surface. The dominant effect can be investigated in future by increasing the Hf sputter coating thickness to further enhance the oxidation and especially nitridation resistance. In the case of Hf, a direct deposition at the surface seems to offer a higher oxidation resistance, decreased spallation, and a lower nitrogen uptake. A

better oxidation performance of coated samples in comparison with alloyed samples is also in agreement with other studies [27, 72, 73]. However, further experiments with respect to the influence of concentration deviations of Hf on alloys as well as coatings should be carried out.

Conclusions

This study showed that the well-known positive effect of RE on the oxidation kinetics and the scale adhesion can also be applied to pure Cr. Oxidation for 50 h at 1050 °C in synthetic air proved high differences between alloying with different RE as well as between different RE supplies such as coatings or alloying. The main conclusions drawn from this are:

- RE alloying decreases the mass gain of Cr during oxidation. Assuming parabolic kinetics, RE addition not only affects the parabolic rate constant but also decreases the linear mass loss.
- A high percentage of mass gain during oxidation arises by Cr₂N formation which can be highly reduced by optimized (element and amount) additions of RE.
- Again, it is shown that the impurity content (percentage and elements) is critical for Cr-based systems. Proper RE additions might play a key issue in impurity gettering and thereby improving the oxidation resistance of systems with lower impurities.
- In the case of Hf, the coating systems seem to have a higher influence on the improvement of the oxidation resistance of Cr as compared to that of the samples prepared upon alloying.
- The precursor ceramic coating has a high potential for applying it in high-temperature applications as apart from SiO₂ it also contains the reactive element Hf.

Acknowledgements The authors thank Melanie Thalheimer and Dr. Gerald Schmidt from High Temperature Materials Group, DECHEMA-Forschungsinstitut, for SEM and EPMA measurements and Bastien Burek from Chemical Technology Group, DECHEMA-Forschungsinstitut, for the assistance in sputtering of the reactive elements. Cong Zhou and Ying Zhan from the Dispersive Solids Group, TU Darmstadt, are thanked for their help with precursor sample preparation. The authors would also like to express their gratitude to the Plansee Group for providing chromium used in this work.

References

1. T. M. Pollock and S. Tin, *Journal of propulsion and power* **22**, 361 (2006).
2. S. E. Plansee (2018). <https://www.plansee.com/de/werkstoffe/chrom.html> Werkstoffe Chrom.
3. A. S. Dorcheh and M. C. Galetz, *JOM* **68**, 2793 (2016).
4. 2017 U.S. Geological Survey. Mineral Commodity Summaries 2017. U.S. Geological Survey, 2017.
5. W. H. Smith and A. U. Seybolt, *Journal of the Electrochemical Society* **103**, 347 (1956).
6. H. B. Goodwin, E. A. Gilbert, C. M. Schwartz and C. T. Greenidge, *Journal of the Electrochemical Society* **100**, 152 (1953).
7. E. A. Brandes, H. T. Greenaway and H. E. N. Stone, *Nature* **178**, 587 (1956).

8. American society for metals, ed. *Ductile Chromium and its Alloys*. (American Society for Metals, 1957).
9. K. Taneichi, T. Narushima, Y. Iguchi and C. Ouchi, *Materials Transactions* **47**, 2540 (2006).
10. A. U. Seybolt and D. H. Haman, *Transactions of the Metallurgical Society of AIME* **230**, 1294 (1964).
11. P. Kofstad, *High Temperature Corrosion*, (Elsevier, London, 1988).
12. E. A. Gulbransen and K. F. Andrew, *Journal of the Electrochemical Society* **99**, 402 (1952).
13. H. Taimatsu, *Journal of the Electrochemical Society* **146**, 3686 (1999).
14. A. M. Dymshits, P. I. Dorogokupets, I. S. Sharygin, K. D. Litasov, A. Shatskiy, S. V. Rashchenko, E. Ohtani, A. Suzuki and Y. Higo, *Physics and Chemistry of Minerals* **43**, 447 (2016).
15. J. A. Haynes, B. A. Pint, W. D. Porter and I. G. Wright, *Materials at High Temperatures* **21**, 87 (2004).
16. P. Kofstad and K. P. Lillerud, *Oxidation of Metals* **17**, 177 (1982).
17. L. B. Pfeil, UK patent No. 574088. 1945.
18. L. B. Pfeil, UK patent No. 459848. 1937.
19. D. Caplan and M. Cohen, *Journal of the Electrochemical Society* **108**, 438 (1961).
20. W. C. Hagel, *Journal of the Electrochemical Society* **109**, C78 (1962).
21. P. Y. Hou, *Materials Science Forum* **696**, 39 (2011).
22. B. A. Pint, Progress in understanding the reactive element effect since the Whittle and Stringer literature review, in *Proceedings John Stringer Symposium on High Temperature Corrosion*, (ASM International Materials Park, Ohio, 2003), p. 9.
23. S. Chevalier, *Materials and Corrosion* **65**, 109 (2014).
24. J. Quadackers and L. Singheiser, *Materials Science Forum* **369**, 77 (2001).
25. J. Stringer, B. A. Wilcox and R. I. Jaffee, *Oxidation of Metals* **5**, 11 (1972).
26. D. P. Whittle and J. Stringer, *Philosophical Transactions of the Royal Society of London A* **295**, 309 (1980).
27. P. Papaiaacovou, R. J. Hussey, D. F. Mitchell and M. J. Graham, *Corrosion Science* **30**, 451 (1990).
28. T. A. Ramanarayanan, R. Ayer, R. Petkovic-Luton and D. P. Leta, *Oxidation of Metals* **29**, 445 (1988).
29. C. M. Cotell, G. J. Yurek, R. J. Hussey, D. F. Mitchell and M. J. Graham, *Oxidation of Metals* **34**, 173 (1990).
30. S. Roure, F. Czerwinski and A. Petric, *Oxidation of Metals* **42**, 75 (1994).
31. W. E. King, J.-H. Park, J. L. Routbort and K. C. Goretta, *Oxidation of Metals* **29**, 217 (1988).
32. Y. Zhang, W. W. Gerberich and D. A. Shores, *Journal of Materials Research* **12**, 697 (1997).
33. D. Zhu, J. H. Stout, J. C. Nelson and D. A. Shores, *Materials Science Forum* **251**, 437 (1997).
34. W. J. Quadackers, *Materials and Corrosion* **41**, 659 (1990).
35. N. Patibandla, T. A. Ramanarayanan and F. Cosandey, *Journal of the Electrochemical Society* **138**, 2176 (1991).
36. K. Przybylski and G. J. Yurek, *Materials Science Forum* **43**, 1 (1989).
37. M. J. Bennett, A. T. Tuson, D. P. Moon, J. M. Titchmarsh, P. Gould and H. M. Flower, *Surface and Coatings Technology* **51**, 65 (1992).
38. L. V. Ramanathan, M. F. Pillis and S. M. C. Fernandes, *Journal of Materials Science* **43**, 530 (2008).
39. S. Chevalier, G. Bonnet, G. Borchardt, J. C. Colson and J. P. Larpin, *Materials Science Forum* **369**, 327 (2001).
40. A. Venskutonis, W. Glatz, and G. Kunschert, P/M processing of ODS Cr-and FeCr-based alloys for solid oxide fuel cell applications, in Proceedings PLANSEE Seminar 2005, PLANSEE SE, 2005.
41. R. J. Hussey and M. J. Graham, *Oxidation of Metals* **45**, 349 (1996).
42. J. Yuan, SiHf(B)CN-based ultra-high temperature ceramic nanocomposites: Single-source precursor synthesis and behavior in hostile environments. Ph.D. thesis, (Technische Universität Darmstadt, 2015).
43. J. Yuan, M. Galetz, X. G. Luan, C. Fasel, R. Riedel and E. Ionescu, *Journal of the European Ceramic Society* **36**, 3021 (2016).
44. I. Smokovych, G. Hasemann, M. Krüger and M. Scheffler, *Journal of the European Ceramic Society* **37**, 4559 (2017).
45. A. Soleimani-Dorcheh, Oxidation-nitridation of chromium at high temperatures and its mitigation by alloying. Ph.D. thesis, RWTH Aachen, (Lehrstuhl und Institut für Eisenhüttenkunde, 2017). RWTH-2017-02157.

46. J. Yuan, S. Hapis, H. Breitzke, Y. Xu, C. Fasel, H.-J. Kleebe, G. Buntkowsky, R. Riedel and E. Ionescu, *Inorganic Chemistry* **53**, 10443 (2014).
47. K. N. Strafford, *Corrosion Science* **19**, 49 (1979).
48. A. S. Dorcheh, M. Schütze and M. C. Galetz, *Corrosion Science* **130**, 261 (2018).
49. C. S. Tedmon, *Journal of the Electrochemical Society* **113**, 766 (1966).
50. A. S. Khanna, *Introduction to High Temperature Oxidation and Corrosion*. (ASM international, 2002).
51. L. Royer, X. Ledoux, S. Mathieu and P. Steinmetz, *Oxidation of Metals* **74**, 79 (2010).
52. J. Yuan, D. Li, K. E. Johanns, C. Fasel, K. Durst, H.-J. Kleebe, Z. Shen, R. Riedel and E. Ionescu, *Journal of the European Ceramic Society* **37**, 5157 (2017).
53. G. Gregori, H.-J. Kleebe, D. W. Readey and G. D. Sorarù, *Journal of the American Ceramic Society* **89**, 1699 (2006).
54. H.-J. Kleebe, K. Nonnenmacher, E. Ionescu and R. Riedel, *Journal of the American Ceramic Society* **95**, 2290 (2012).
55. K. Nonnenmacher, H.-J. Kleebe, J. Rohrer, E. Ionescu and R. Riedel, *Journal of the American Ceramic Society* **96**, 2058 (2013).
56. Q. Wen, R. Riedel and E. Ionescu, *Corrosion Science* **145**, 191 (2018).
57. Q. Wen, R. Riedel and E. Ionescu, *Advanced Engineering Materials* **21**, 1800879 (2019).
58. G. Hultquist, B. Tveten and E. Hörnlund, *Oxidation of Metals* **54**, 1 (2000).
59. M. Michalik, M. Hänsel, and W. J. Quadackers, Effect of water vapour on growth and adherence of chromia scales on pure chromium. Ph.D. thesis, (Forschungszentrum Jülich, Zentralbibliothek, 2007).
60. P. Y. Hou and J. Stringer, *Oxidation of Metals* **38**, 323 (1992).
61. M. S. Li and P. Y. Hou, *Acta Materialia* **55**, 443 (2007).
62. F. Czerwinski and W. W. Smeltzer, *Oxidation of Metals* **40**, 503 (1993).
63. K. Przybylski, A. J. Garratt-Reed, B. A. Pint, E. P. Katz and G. J. Yurek, *Journal of the Electrochemical Society* **134**, 3207 (1987).
64. N. Birks, G. H. Meier and F. S. Pettit, *Introduction to the high temperature oxidation of metals*, (Cambridge University Press, 2006).
65. G. J. Yurek, K. Przybylski and A. J. Garratt-Reed, *Journal of the Electrochemical Society* **134**, 2643 (1987).
66. S. Chevalier, G. Bonnet, K. Przybylski, J. C. Colson and J. P. Larpin, *Oxidation of Metals* **54**, 527 (2000).
67. A. Ul-Hamid, *Oxidation of Metals* **58**, 23 (2002).
68. A. Solimani, M. Schütze, A. Stark, Andreas and M. C. Galetz, *Corrosion Science* **145**, 180 (2018).
69. J. Klöwer and J.-G. Li, *Materials and Corrosion* **47**, 545 (1996).
70. D. J. Young, T. D. Nguyen, P. Felfer, J. Zhang and J. M. Cairney, *Scripta Materialia* **77**, 29 (2014).
71. A. Soleimani-Dorcheh, W. Donner and M. C. Galetz, *Materials and Corrosion* **65**, 1143 (2014).
72. P. Y. Hou and J. Stringer, *Journal of the Electrochemical Society* **134**, 1836 (1987).
73. P. Y. Hou, Z. R. Shui, G. Y. Chuang and J. Stringer, *Journal of The Electrochemical Society* **139**, 1119 (1992).

Publisher's Note Springer Nature remains neutral with regard to jurisdictional claims in published maps and institutional affiliations.